



1 **Role of black carbons mass size distribution in the direct aerosol radiative forcing**

2 Gang Zhao¹, Jiangchuan Tao², Ye Kuang², Chuanyang Shen¹, Yingli Yu¹, Chunsheng Zhao^{1*}

3 ¹Department of Atmospheric and Oceanic Sciences, School of Physics, Peking University, Beijing,
4 China

5 ²Institute for Environmental and Climate Research, Jinan University, Guangzhou 511443, China

6 **Correspondence to: Chunsheng Zhao (zcs@pku.edu.cn)*

7 **Abstract**

8 Large uncertainties exist when estimating radiative effects of ambient black carbon (BC) aerosol.
9 Previous studies about the BC aerosol radiative forcing mainly focus on the BC aerosols' mass
10 concentrations and mixing states, while the effects of BC mass size distribution (BCMSD) were not
11 well considered. In this paper, we developed a method by measuring the BCMSD by using a
12 differential mobility analyzer in tandem with an aethalometer. A comprehensive method of multiple
13 charging corrections was proposed and implemented in measuring the BCMSD. Good agreement
14 was obtained between the BC mass concentration integrated from this system and that measured in
15 bulk phase, demonstrating the reliability of our proposed method. Characteristics of the BCMSD and
16 corresponding radiative effects were studied based on field measurements conducted in the North
17 China Plain by using our own designed measurement system. Results showed that the BCMSD had
18 two modes and the mean peak diameters of the two modes were 150 nm and 503 nm respectively.
19 The BCMSD of coarser mode varied significantly under different pollution conditions with peak
20 diameter varying between 430 nm and 580 nm, which gave rise to significant variation in aerosol
21 buck optical properties. The aerosol direct aerosol radiative forcing was estimated to vary by 22.5%
22 for different measured BCMSDs, which shared the same magnitude to the variation associated with
23 assuming different aerosol mixing states (21.5%). Our study reveals that the BCMSD matters as well
24 as their mixing state in estimating the direct aerosol radiative forcing. Knowledge of the BCMSD
25 should be fully considered in climate models.

26 **1 Introduction**

27 Atmospheric black carbon (BC) is the second strongest absorbing components in atmosphere
28 (Bond et al., 2013) but the magnitudes of the warming effects are poorly quantified. When emitted to
29 the surrounding, BC particles transform the morphology from fractal to spherical and then grow as
30 fully compact particles with other components depositing on the BC aerosol (Peng et al., 2016). The



31 variation in the shapes of BC aerosols, together with the variation in the mixing states, can lead to
32 substantial change of aerosol optical properties (Liu et al., 2017;China et al., 2013;Wu et al.,
33 2016a;Wu et al., 2018). BC aerosols also have significant influence on the climate by interacting
34 with clouds (Koch and Del Genio, 2010;Roberts et al., 2008;Stevens and Feingold, 2009), ice and
35 snow (Bond et al., 2013). Recent study shows that the solar absorption of BC can suppress the
36 turbulence in the atmospheric boundary layer (Wilcox et al., 2016). It is found that BC emissions
37 may be responsible for the incensement of droughts and floods in China and India (Menon et al.,
38 2002). In addition, BC can pose a serve threat to human health through inhalation (Nichols et al.,
39 2013;Janssen et al., 2011).

40 Comprehensive studies have been carried out to evaluate the climate effect of BC based on the
41 measurement of BC mass concentrations (m_{BC}) (Koch et al., 2009;Ramanathan and Carmichael,
42 2008). The m_{BC} near the ground have been well characterized (Ramachandran and Rajesh,
43 2007;Ran et al., 2016b;Reddington et al., 2013;Song et al., 2013), and the BC vertical distributions
44 are widely measured and evaluated as well (Ran et al., 2016a;Babu et al., 2011;Ferrero et al., 2011).
45 Despite these measurements, more insights into the BC microphysical properties can help to estimate
46 the influence of BC aerosols on visibility (Zhang et al., 2008), climate (Jacobson, 2001) and human
47 health (Lippmann and Albert, 1969). These microphysical properties include BC morphology (Zhang
48 et al., 2016), density (Zhang et al., 2016), complex refractive index (Bond et al., 2013), mixing states
49 (Moffet et al., 2016;Raatikainen et al., 2017), and particularly, the mass size distribution (BCMSD)
50 (Cheng et al., 2012;Cheng and Yang, 2016;Gong et al., 2016). Knowledge of BCMSD is not only
51 helpful to study the mixing state of BC aerosols (Raatikainen et al., 2017), but also essential to model
52 the role of BC in evaluating regional and global climate accurately (Huang and Yu, 2008b). BC
53 radiative effects is highly sensitive to the emitted BC particle size distribution (Matsui et al., 2018).
54 The health impacts of BC are significantly related to BCMSD (Turner et al., 2015). Furthermore, the
55 information of BCMSD can help to study the source, the evolution and the mixing state of ambient
56 BC aerosols (Yu et al., 2010). However, few studies have focused on the characteristics of the
57 BCMSD, and the BCMSD properties under different polluted conditions are not known yet.

58 Many methods have been proposed to measure the BCMSD. For instance, the BCMSD was
59 measured by sampling the aerosol in the size range from about 50 nm to several micrometers onto
60 quartz fiber filter substrates using a micro-orifice uniform deposit impactor (MOUDI) (Huang and



61 Yu, 2008b;Venkataraman and Friedlander, 1994;Guo, 2016). Cheng et al. (2014) developed a method
62 to measure the BCMSD by employing two aethalometers in parallel, with one to measure total m_{BC}
63 and the other to measure m_{BC} below specific particle sizes using a size cut-off inlet. The Single
64 Particle Soot Photometer (SP2) is developed and widely used because it provides single particle
65 information, hence the BCMSD and the mixing state of the atmospheric aerosols can be derived
66 directly (Schwarz et al., 2006;Gao et al., 2007;Huang et al., 2012;Singh et al., 2016). However, the
67 laser-induced incandescence method cannot provide reliable information about the particles beyond
68 the range of 70 nm and 400 nm (Moteki and Kondo, 2010), which results in the lack of the
69 knowledge of the BCMSD characteristics for these aerosols over 400 nm. The results from MOUDI
70 find that a great amount of BC locates at the diameter range larger than 370nm (Wang et al., 2015;Hu
71 et al., 2012). However, the measurements of MOUDI cannot give detailed information of the
72 BCMSD evolution due to the low temporal and diameter resolution (Xiaofeng Huang et al., 2006).
73 The characteristics of the BCMSD larger than 370 nm is not well studied due to the limitation of the
74 instrument.

75 Recently, Ning et al. (2013) and Stabile et al. (2012) proposed a new method to measure the
76 BCMSD by using differential mobility analyzer (DMA) in tandem with Aethalometer (AE). This
77 method has the potential of measuring the BCMSD from 20 nm to 584 nm with high time resolution.
78 We develop and validate the BCMSD measurement system based on the works of Ning et al. (2013).
79 The developed measurement system was employed in a field campaign in the North China Plain. The
80 characteristics of the measured BCMSD were studied based on the field measurement. Furthermore,
81 the effects of BCMSD variations on the aerosol optical properties and corresponding direct aerosol
82 radiative properties were evaluated. The aerosol optical properties were calculated by using the Mie
83 scattering theory. The direct aerosol radiative forcing (DARF) were estimated by using the Santa
84 Barbara DISORT (discrete ordinates radiative transfer) Atmospheric Radiative Transfer (SBDART)
85 model.

86 The structure of this paper are organized as follows. Section 2 gives the information about the
87 instrument setup and field measurement. Section 3 gives the detailed method used in this study,
88 which contains: 1, conducting multiple charging corrections when deriving the aerosol BCMSD and
89 2, evaluating the aerosol optical and radiative properties for different BCMSD. Results and
90 discussions are shown in section 4. The conclusion is drawn in the last part.



91 2 Instrument Setup

92 The measurement system setup was based on the works of Stabile et al. (2012) and Ning et al.
93 (2013) as schematically shown in Fig.1. The ambient sample aerosol particles were firstly dried to
94 below relative humidity of 30% through a Nafion drying tube before passing through to the DMA
95 (Model 3081, TSI, USA). The DMA scanned aerosol particles with diameter ranges from 12.3 to 697
96 nm over a period of 285 seconds and started another scanning after a pause of 15 seconds, so one
97 complete cycle took 5 minutes. The sheath and sample flow rates of the DMA were 3 lpm and 0.5
98 lpm, respectively. The quasi-monodisperse aerosols that passed through the DMA were further
99 divided into two flows: with one lead to an aethalometer (AE51, Model 51, MicroAeth, USA) with a
100 flow rate of 0.2 lpm to measure the m_{BC} at 1 second time resolution; and the other one with flow
101 rate of 0.3 lpm flow directed to a CPC (Model 3772, TSI, USA), which counted particle number
102 concentrations at 0.1 second resolution. Clean air with a flow rate of 0.7 lpm was used to compensate
103 for the CPC inlet flow, which had default flow rate of 1 lpm. Overall, the combination system of
104 DMA, CPC and AE51 could provide one PNSD and BCMSD scan every 5 minutes.

105 At the same time, another aethalometer (AE33, Model 33, Magee, USA) was used to measure
106 the m_{BC} with a time resolution of 1 minute. The mass concentration of particles with diameter
107 smaller than 2.5 μm (PM_{2.5}) was concurrently measured with time resolution of 1 minute during the
108 filed observations by the Tapered Element Oscillating Microbalance (TEOM) Dichotomous Ambient
109 Particulate Monitor (1405-DF), which was an indicator of the pollution conditions.

110 From 21 March to 9 April in 2017, an intensive field measurement was conducted to
111 characterize of the ambient aerosol BCMSD at the AERONET BEIJING_PKU station (N39°59',
112 E116°18'). This station was located on one roof of Peking University campus in the north west of
113 Beijing, China. There were two main streets, Chengfu Road to the south and Zhongguancun Street to
114 the west that surrounding the station. The aerosol sampled at this station were mainly composed of
115 urban roadside aerosols (Zhao et al., 2018).

116 3 Methodologies

117 3.1 Retrieving the BCMSD

118 Four steps were involved to calculate the BCMSD using the raw data from the measurement
119 system: 1), correcting the 'loading effect' of m_{BC} measured by AE51; 2), matching the instrument
120 time between the AE51 and CPC; 3), matching the measured m_{BC} and diameter to get the raw



121 BCMSD that is not involved in multiple charging corrections; 4), conducting the multiple charging
122 corrections of the measured raw BCMSD.

123 3.1.1 Obtaining the raw BCMSD

124 The aethalometer (AE51 and AE33) is a well-developed and widely used instrument to measure
125 the m_{BC} (Drinovec et al., 2015; Hansen et al., 1984). When absorbing aerosols accumulates on the
126 sample filter of the aethalometer continuously, the m_{BC} can be determined by concurrently
127 measuring the light intensities I after the fiber filter and the light intensities I_0 transmitted through
128 reference spot which is free of aerosol loading. The light attenuation (ATN) is defined as:

$$129 \quad \text{ATN} = 100 \cdot \ln\left(\frac{I_0}{I}\right). \quad (1)$$

130 The mass of BC loaded on the filter is given by:

$$131 \quad m_{BC,load} = \frac{A \cdot \text{ATN}}{100 \cdot \sigma_{BC}}, \quad (2)$$

132 where A is the sample spot area on the filter and σ_{BC} is the mass attenuation cross-section of BC.
133 The equivalent m_{BC} can be calculated through the increment of $m_{BC,all}$:

$$134 \quad m_{BC} = \frac{m_{BC,load}}{\Delta t} = \frac{A \cdot \Delta \text{ATN}}{100 \cdot \sigma_{BC} \cdot F \cdot \Delta t}, \quad (3)$$

135 where F is the flow rate and ΔATN is the ATN variation during the time period of Δt .

136 Corrections of the measured m_{BC} are necessary because the systematic bias exists due to the
137 prevalingly known ‘loading effect’ (Drinovec et al., 2015; Virkkula et al., 2015; Virkkula et al., 2007).
138 The AE33 can directly provide the corrected m_{BC} values through measuring two light intensities of
139 two spots with different BC load efficiencies (Drinovec et al., 2015). For AE51, The correcting
140 method in Virkkula et al. (2007) was adopted:

$$141 \quad m_{BC,corrected} = (1 + k \times \text{ATN}) m_{BC,uncorrected}, \quad (4)$$

142 where k is the correction factor and a constant value of 0.004 is employed in this study to correct
143 the m_{BC} from AE51. In the first part of the supplementary material, we showed that the loading
144 effects corrections of m_{BC} from AE51 were essential and the value of m_{BC} from AE33 could be
145 used as a reference for the measured BCMSD.

146 Time correction was needed because time gaps between voltages implied on the DMA (particle
147 size) and sample particles measured by different instruments were not the same. The time correction
148 procedures were conducted every day during the field measurement to ensure that the time deviations
149 of the CPC and the AE51 were constrained within 2 seconds.



150 Fig. S3 gave the time series diagram of scanned aerosol diameters by DMA, measured m_{BC}
151 from AE51, and the aerosol number concentrations counted by CPC. The aerosol PNSD (or BCMSD)
152 could be calculated by matching the DMA diameter and the measured aerosol number concentrations
153 (or measured m_{BC}) by simply using the single particle charge ratio for each electrical mobility
154 diameter. These measured PNSD and BCMSD did not consider the effect of multiple-charging
155 corrections and are labeled as raw aerosol PNSD and raw aerosol BCMSD.

156 3.1.2 Multiple charging corrections of raw BCMSD

157 In the work of Ning et al. (2013) study, lots of efforts were made to evaluate the performance of
158 the instrument. They considered the diffusion corrections and particle charging corrections. However,
159 the particle charging corrections were limited to single particle charge ratio as they mentioned that
160 they simplified the particle charge correction by applying the peak electrical mobility for the
161 calculation of representative particle size for each mobility bin and single particle charge ratio for
162 each primary mobility. They ignored the fact that the aerosol samples selected by the DMA were
163 quasi-monodisperse with different charges and different diameters.

164 We proposed a new algorithm for the multi-charge corrections of the BCMSD. Multi-charge
165 corrections to the measured size distribution were prevailing when the DMA was used to scan the
166 aerosol sizes. When the DMA and CPC are used together to measure the aerosol particle number size
167 distribution (PNSD), the multi-charging corrected aerosol PNSD can be significantly different from
168 the raw measured one (Bau et al., 2014; He and Dhaniyala, 2013; He et al., 2015). As shown in the
169 results part of this study, the multi-charge corrections of the BCMSD could cause differences in both
170 the magnitude and shape of the BCMSD. Therefore, it is necessary to perform multi-charge
171 corrections on the BCMSD. This study developed a new algorithm to correct the m_{BC} from
172 measured m_{BC} based on the work of Hagen and Alofs (2007) and Deng et al. (2011).

173 When the DMA is charged with a negative voltage, those aerosols with a small range of
174 electrical mobility (Z_p) can pass through the DMA:

$$175 \quad Z_p = \frac{q_{sh}}{2\pi VL} \ln\left(\frac{r_1}{r_2}\right), \quad (5)$$

176 where q_{sh} is the sheath air flow rate; V is the average voltage on the inner center rod; r_1 and r_2
177 are the outer and inner radius of annular space respectively. The Z_p is related with D_p by
178 elementary charge (e), number of elementary charges on the particle (n), and gas viscosity poise (μ)



179 with:

$$180 \quad Z_p = \frac{neC(D_p)}{3\pi\mu D_p}, \quad (6)$$

181 where $C(D_p)$ is Cunningham slip correction:

$$182 \quad C = 1 + \frac{2\tau}{D_p} \left(1.142 + 0.558e^{-\frac{0.999D_p}{2\tau}} \right), \quad (7)$$

183 where τ is the gas mean free path. From equation 7, aerosol particles can have the same Z_p despite
184 that they have different n and D_p . At the same time, there exists a relatively larger portion of
185 multiple charged particles for those particles with diameters between 100 nm and 400 nm when the
186 ambient aerosols pass through the X-ray (Tigges et al., 2015; Wiedensohler and Fissan, 1988).
187 Through the above discussion, the selected aerosols by DMA at a given electrical mobility can have
188 different charges which will correspond to different diameters.

189 When the scan diameter is set as D_{p_i} for the singly charged particles and the respective voltage
190 of DMA is V_i ($i=1, 2, \dots, I$), aerosol particles with electro-mobility of $Z_{p,i}$ ($i=1, 2, \dots, I$) can pass
191 through the DMA and the observed m_{BC} by AE51 can be expressed as:

$$192 \quad R_i = \int_0^\infty G(i, x) A(x) n(x) dx, \quad (8)$$

193 where x is the scale parameter, with the definition of $x = \log(D_{p_i})$, $A(x)$ is the average BC mass
194 concentration of single particles for scale parameter x , and $n(x) = dN/d\log D_p$ is aerosol PNSD
195 that is the multiple charging corrected results from the measured aerosol PNSD. We define the kernel
196 function $G(i, x)$, which is crucial to the algorithm, as:

$$197 \quad G(i, x) = \sum_{v=1}^\infty \phi(x, v) \Omega(x, v, i), \quad (9)$$

198 where $\phi(x, v)$ is the probability of particles that are charged with v charges at the scale parameter
199 of x (Wiedensohler, 1988). $\Omega(x, v, i)$ is the probability of particles that can pass through the DMA
200 with v charges at the scale parameter x (Knutson and Whitby, 1975). In this study, the maximum
201 value of v is 10.

202 The multiple charging corrections can be expressed as computing the $A(x_i^*)$, in which x_i^* is the
203 predetermined scale parameter from the DMA. To get the numerical integration results of equation 9,
204 the diameter interval that is 1/50 of the measured diameter is used. Thus, equation 9 can be written as

$$205 \quad R_i = \int_0^\infty G(i, x) A(x) n(x) dx = \Delta x_i \sum_{j=1}^{50} \beta_j G(i, x_{i,j}) A(x_{i,j}) n(x_{i,j}), \quad (10)$$

206 where $\beta = \begin{cases} 0.5, & j = 1, J \\ 1, & \text{otherwise} \end{cases}$; $x_{i,j}$ is the j^{th} ($j=1, 2, \dots, 50$) parameter that locates at the parameter x_i and



207 x_{i+1} and $A(x_{i,j})$ ($i=1, 2, \dots, I; j=1, 2, \dots, 50$), the BC mass ratio at scale parameter $x_{i,j}$, is expressed
208 as the linear interpolation of the values at the measured diameters.

$$209 \quad A(x_{i,j}) = A(x_i) + P_i(x_{i,j} - x_i), \quad (11)$$

210 where P_i is the slope of the linear interpolation result of

$$211 \quad A(x_k^*) = C + P_i \cdot x_k^*. \quad (12)$$

212 x_k^* refers to these five diameters that are nearest to the predetermined scale parameter x_i . C is the
213 intercept of the linear interpolation result.

214 With $H_{i,j} = \beta_j \Delta x_i G(i, x_{i,j}) n(x_{i,j})$, equation 11 can be written as

$$\begin{aligned} 215 \quad R_i &= \sum_{j=1}^J H_{ij} [A(x_i) + P_i(x_{i,j} - x_i)] = \sum_{j=1}^J H_{ij} A(x_i) + \sum_{j=1}^J H_{ij} P_i x_{i,j} - \sum_{j=1}^J H_{ij} P_i x_i \\ 216 \quad &= \sum_{k=1}^I (\sum_{j=1}^J H_{ij} \delta(i-k)) A(x_k^*) + \sum_{k=1}^I (\sum_{j=1}^J H_{ij} x_{i,j} \delta(i-k)) P_k - \sum_{k=1}^I \delta(i-k) P_k x_k^* \\ 217 \quad &= \sum_{k=1}^I Q_{ik} A(x_k^*) + \sum_{k=1}^I T_{ik} P_k - \sum_{k=1}^I Q_{ik} P_k x_k^*, \quad (13) \end{aligned}$$

218 where $\delta(x) = \begin{cases} 0, & x \neq 0 \\ 1, & x = 0 \end{cases}$,

$$219 \quad Q_{ik} = \sum_{j=1}^J H_{ij} \delta(i-k), \quad (14)$$

$$220 \quad \text{and } T_{ik} = \sum_{j=1}^J H_{ij} x_{i,j} \delta(i-k). \quad (15)$$

221 By letting the

$$222 \quad S_i = R_i - \sum_{k=1}^I T_{ik} P_k + \sum_{k=1}^I Q_{ik} P_k x_k^*. \quad (16)$$

223 This equation is then expressed as

$$224 \quad S_i = \sum_{k=1}^I Q_{ik} A(x_k^*), \quad (17)$$

225 or

$$226 \quad S = QA, \quad (18)$$

227 where S and A are $I \times 1$ vectors and Q is an $I \times I$ matrix. This matrix can be solved by using the
228 non-negative least square method.

229 Finally, the $A(x)$ can be determined and the corresponding BCMSD that is multiple charging
230 corrected can be calculated.

231 3.1.3 Validation of the multiple charging corrections

232 An example of the multiple charging corrections was shown in Fig. 2. The corrections of aerosol
233 PNSD were based on the work of Hagen and Alofs (2007). As shown in Fig. 2(a), the corrected



234 aerosol PNSD was significantly different from the original uncorrected one. There were about half of
235 the measured particles have multiple elementary charge in the size range between 100 and 200 nm.
236 The raw uncorrected aerosol PNSD had a peak value of 10920 cm^{-3} at 98 nm while the corrected
237 aerosol PNSD reached its peak value of 8450 cm^{-3} at 98 nm. The peak positions of the raw aerosol
238 particle mass size distribution (PMSD, dm/dlogD_p) peaked at 371 nm with a peak value of $56 \mu\text{g}/\text{m}^3$
239 and the corrected aerosol PMSD had a peak value of $53 \mu\text{g}/\text{m}^3$ at 445 nm. The peak position of the
240 aerosol PMSD shifted a lot before and after the multiple charging corrections. The similar case for
241 the BCMSD was shown in Fig. 2(b). The shape of BCMSD had changed substantially due to the
242 multiple charging corrections. The measured raw BCMSD had a peak diameter near 300 nm and the
243 magnitude of BCMSD plateau reached $6000 \text{ ng}/\text{m}^3$ at 283 nm, which was in accordance with the
244 results of Ning et al. (2013), where the multiple charging corrections were not involved. However,
245 the corrected BCMSD peaks near 400 nm, with a peak value of about $5500 \text{ ng}/\text{m}^3$ at 407 nm.
246 According to the result, a small amount of BC remained in particles with diameter between 100 nm
247 and 200 nm. The measured BCMSD changed a lot when multiple charging corrections were
248 implemented, which highlighted the necessity of implementation of appropriate multiple charging
249 corrections

250 The m_{BC} integrated from measured BCPMSD changed after multiple charging corrections. Fig.
251 S4 showed the comparison results of the m_{BC} measured by AE33 and the m_{BC} integrated from
252 AE51 measurements. The m_{BC} integrated from uncorrected and corrected BCMSD versus m_{BC}
253 measured by AE33 were shown in Fig.S4(a) and Fig.S4(b), respectively. Before multiple charging
254 corrections, the m_{BC} from uncorrected BCPMSD increased linearly with the m_{BC} from AE33, with
255 R^2 equaling 0.87, but it was 2.37 times that of AE33 in average. As a comparison, overall magnitude
256 of m_{BC} integrated from corrected BCPMSD agreed better with that from AE33 with a slope of 1.2.
257 With the discussion above, multiple charging corrections were essential for BCMSD measurements.

258 3.2 Fitting the BCMSD by using two log-normal models

259 Based on the measurement results, the BCMSD had two modes for most of the conditions. The
260 BCMSD are assumed to be of two log-normal distributions as:

$$261 m_{fit,D_p} = \sum_{i=1,2} \frac{m_i}{\sqrt{2\pi \log(GSD_i)}} \cdot \exp\left(-\frac{[\log(D_p) - \log(D_{m,i})]^2}{2 \log^2(GSD_i)}\right), \quad (19)$$

262 Where D_p is the diameter of the aerosols; m_i is the mass of mode i ($i=1,2$); GSD_i is the geometric



263 standard deviation at mode i ($i=1,2$), and $D_{m,i}$ is the geometric mean diameter of the mode i ($i=1,2$).
264 The GSD_i and $D_{m,i}$ can be determined by using the least square method with the objective function
265 as :

$$266 \quad J = \sum_{i=1,n} (m_{Dp_i} - m_{fit,Dp_i}(D_{m1}, GSD_1, D_{m2}, GSD_2))^2, \quad (20)$$

267 Where m_{Dp_i} is the measured mass distribution at Dp_i , while m_{fit,Dp_i} is the fit mass distribution at
268 Dp_i .

269 3.3 Estimating aerosol optical properties with different BCMSD

270 The Mie scattering model was used to study the influence of the BCMSD variation on the aerosol
271 optical properties. When running the Mie model, aerosol PNSD and BC were necessary. The aerosol
272 PNSD and m_{BC} used here is the mean result of aerosol PNSD and m_{BC} over the whole field
273 measurement respectively. The amount of BC particle adopted in this study is the mean value of the
274 m_{BC} measured by AE33. In this study, The BCMSD was assumed to be log-normal distributed. D_m
275 of the BCMSD was set to vary from 100 nm to 600 nm. GSD of the BCMSD was set to be in the
276 range between 1.3 and 1.8. BC was treated as partially externally mixed and the remaining aerosols
277 was treated as core-shell mixed. The ratio of externally mixed m_{BC} to core-shell m_{BC} was
278 determined by the method introduced in Ma et al. (2012) and a mean ratio of 0.51 was used. The
279 density and refractive index of BC were set as 1.5 g/cm³ and 1.8+0.54i (Kuang et al., 2015),
280 respectively. The complex refractive index of non-absorbing aerosols was 1.53+10⁻⁷i (Wex et al.,
281 2002) at the wavelength of 525 nm. More details of calculating the aerosol optical properties by
282 using the aerosol PNSD and BCMSD, can refer to Kuang et al. (2016). For each BCMSD, extinction
283 coefficient (σ_{ext}), the scattering coefficient (σ_{sca}), the single scattering albedo (SSA), and the
284 asymmetry factor (g) could be obtained from the output of Mie scattering model.

285 3.4 Evaluating the DARF

286 In this study, the SBDART model (Ricchiazzi et al., 1998) was employed to estimate the DARF.
287 In our study, the instantaneous DARF for cloud free conditions at the top of atmosphere was
288 calculated. Input of the model required the profiles of aerosol σ_{ext} , SSA, g . These values were
289 calculated by parameterized aerosol PNSD, BCMSD profiles. The corresponding DARF for different
290 BCMSD could be estimated. More details of estimating the DARF could refer to part 4 and 5 in the



291 supplementary material. The DARF was estimated for the measured mean aerosol PNSD and m_{BC}
292 under different BCMSD conditions to study the effects of BCMSD variations on the aerosol DARF.

293 **4 Results and Discussions**

294 **4.1 Measurement results of the BCMSD**

295 The time series of measured PM_{2.5}, aerosol PNSD and BCMSD were shown in Fig. 3. During
296 the observation period, the PM_{2.5} varied from 0.06 to 220 $\mu\text{g}/\text{m}^3$, with a mean value of 71.5 ± 52.56
297 $\mu\text{g}/\text{m}^3$. Three periods of heavy PM_{2.5} loading were observed: (1) PM_{2.5} increased from around 100
298 $\mu\text{g}/\text{m}^3$ to 200 $\mu\text{g}/\text{m}^3$ and decreased slowly to 1 $\mu\text{g}/\text{m}^3$ in the period 21-26, March; (2) the PM_{2.5}
299 accumulated slowly from 28 to 30, March and dissipated quickly from 30, March to 1, April; (3) the
300 rapid accumulation and dissipation of PM_{2.5} happened during 2 to 5, April. During the last five days,
301 PM_{2.5} fluctuated between 20 and 120 $\mu\text{g}/\text{m}^3$. For each pollution condition, both the aerosol total
302 number concentrations and the aerosol median diameter increased. The aerosol median diameter
303 varied between 31 nm and 169 nm with a mean value of 78 ± 31 nm.

304 As for the BCMSD, a distribution with two modes could be detected. The presence of the first
305 mode in the size range between 100 and 200 nm provided a verification of previous field
306 measurements that the BC concentrated in the particle diameter range from 100 to 200 nm. (Huang et
307 al., 2012; Ohata et al., 2011; Wu et al., 2016b). The peak diameter of second mode ranged from 300
308 nm to 600 nm, which agrees well with the measured BCMSD by MOUDI (Klaus Willeke and Baron,
309 1996; Yu and Yu, 2009; Huang and Yu, 2008a). The main BC mass loading was in the coarser mode
310 for the sampled particles when comparing the BC mass concentrations at two modes.

311 The total m_{BC} measured by AE33 ranged from 0.1 to 14 $\mu\text{g}/\text{m}^3$ with an average of 5.04 ± 2.64
312 $\mu\text{g}/\text{m}^3$. Good consistence was achieved between m_{BC} measured by AE33 and m_{BC} calculated from
313 measured BCMSD as shown in Fig. 4(c).

314 **4.2 Evolution of the BCMSD under different polluted conditions**

315 Log-normal distribution was used to fit each mode of the BCMSD by using the least square
316 method as introduced in section 3.2. For each mode, the geometric mean diameter (D_m) and the
317 geometric standard deviation (GSD) of the BCMSD were studied.

318 During the measurement period, both D_m and GSD of the two modes had changed significantly
319 as shown in Fig 4. The D_m of first and second mode varied from 128 to 162 nm and from 430 to



320 580 nm, respectively. The corresponding mean D_m was 150 and 503 nm. The D_m of the two
321 modes was found to be positive correlated in Fig. 4a. When the pollution was released from the
322 beginning to 27, March, the D_m decreased from 590 to 420 nm and from 155 to 130 nm for the
323 coarser mode and the smaller mode respectively. The BC containing aerosols tended to be aged and
324 grew larger when the air surrounding get polluted.

325 GSD for the coarser mode and the smaller mode showed very different properties as shown in
326 Fig. 4b. For the second mode, GSD varied from around 1.49 to 1.68 with a mean value of 1.57. The
327 GSD get decreased with the pollution condition, which indicated that BC containing aerosols tend to
328 accumulate to a small range of diameters during the aging processing. This phenomenon was
329 consistent with the fact that larger particles grew relative slower in diameter. For the first mode, GSD
330 ranged from 1.5 to around 1.85 with a mean value of 1.62. However, GSD of the smaller mode tend
331 to be larger when the surrounding air get cleaner, which might be related to the complex sources of
332 the BC emission. A small amount of fresh emitted BC particles can have substantial influence on the
333 mass size distribution of the smaller mode because the BC concentrations of the smaller mode were
334 small, especially under clean conditions. In general, the GSD of coarser mode was a good indicator
335 of the BC aging process and that of the smaller mode could partially reflect the complex sources of
336 the BC fine particles.

337 The relationship between the D_m and the GSD for coarse mode was further analyzed by
338 analyzing the distribution of the D_m and GSD. The GSD and D_m had opposite trends as shown in
339 Fig 5. With the increment of the D_m from 420 to 540 nm, the mean value of GSD decreased from
340 around 1.605 to 1.548 while the m_{BC} increased with the D_m . The statistical relationship between
341 D_m and GSD offered a reasonable representation of the BCMSD under different polluted conditions.
342 In the following work, mean values of the GSD at different D_m were used to for further discussion.

343 Note that the GSD get slightly increased with the increment of D_m when D_m was larger than
344 520 nm. This might be caused by the limit diameter range of BCMSD measuring system which was
345 from 20 to 680 nm. The multiple charge corrections applied to the BCMSD could influence the
346 BCMSD when D_m of the BCMSD was near the end of the scanned diameter and may lead to
347 significant uncertainties to the BCMSD. The measurement results indicated that cases of measured
348 D_m of BCMSD larger than 520 nm were few, demonstrating that this multiple correction effect
349 influenced little on shape of measured BCMSD in most cases.



350 **4.3 Influence of BCMSD variation on the aerosol optical properties**

351 The aerosol optical parameters corresponding to different GSD and D_m values were shown in
352 Fig. 6. In Fig. 6(a), the aerosol g varied from 0.617 to 0.649 (variation of 5.8%). Recent work by
353 Zhao et al, 2017 showed that the aerosol g value in the NCP may vary at a range of 10% due to the
354 change of aerosol PNSD. Aerosol g was more sensitive to D_m when the geometric mean diameter of
355 the BCMSD was lower than 400 nm. However, when the D_m was larger than 400 nm, the g become
356 sensitive to both the D_m and the GSD of BCMSD. Overall, the g varied a little bit (0.617 to 0.624)
357 under the representative conditions during the measurement period. For the aerosol SSA, it was
358 sensitive to the D_m over the whole range as shown in Fig. 6(b). SSA varied between 0.86 and 0.88
359 under the representative measurement conditions. The σ_{sca} had large changes from 264 Mm^{-1} to 313
360 Mm^{-1} . The σ_{sca} was quite sensitive to variations in BCMSD when the D_m was lower than 400 nm as
361 shown in Fig.6c, which varied substantially from 264 Mm^{-1} to 313 Mm^{-1} . In addition, variations in
362 σ_{sca} relied more on the variations in D_m when D_m was larger than 400 nm. Within the measurement
363 conditions of BCMSD, the σ_{sca} varied from 265 Mm^{-1} to 280 Mm^{-1} . The measured GSD under
364 different D_m went along with the gradient direction of the σ_{sca} , which mean that the evolution of
365 BCMSD in the atmosphere influenced substantially on σ_{sca} . As for the σ_{abs} , it changed from 21.94
366 Mm^{-1} to 44.12 Mm^{-1} and the corresponding mass absorption cross section (MAC) was estimated to
367 be in the range of 4.75 to 9.56 m^2/g , suggesting that MAC of the BC aerosols should be carefully
368 studied under different BCMSD conditions.

369 **4.4 Influence of BCMSD on the direct aerosol radiative forcing**

370 The estimated DARF values for different GSD and D_m conditions were estimated. When
371 estimating the DARF, the measured mean aerosol PNSD and mean BC mass concentration were
372 used. The results of estimated DARF were shown in Fig. 7(a). DARF at the surface varied from
373 -4.90 w/m^2 to -2.02 w/m^2 for different BCMSD. Within the measured BCMSD range, the DARF
374 varied from -2.04 w/m^2 to -2.5 w/m^2 , which corresponding to 22.5% of variation. The heating rate
375 within the mixed layer was a powerful indicator of the BC particles' absorbing effects, which may
376 help evaluate the development of the boundary layer. The calculated mean heating rate within the
377 mixed layer changed from 3.25 K/day to 3.89 K/day for different D_m and GSD, as shown in Fig.
378 7(b). The heating rate with the measured BCMSD range could change from 3.56 to 3.75 with a
379 variation of 5.23%.



380 Mixing states of BC play significant roles in calculations of aerosol optical properties and
381 estimations of DARF (Jacobson, 2001). As a comparison, we estimated the DARF under different
382 conditions of BC mixing state: (1) internally mixed, (2) externally mixed and (3) core-shell mixed.
383 Table 1 gave the estimated DARF and mean heating rate within the mixed layer under different
384 mixing state conditions. Results showed that the DARF under different BC mixing states conditions
385 may change by 21.5%, which shared the same magnitude with 22.5% variation of DARF caused by
386 BCMSD variations. In addition, the heating rate was estimated to vary by 6.05%. These results
387 highlighted that the BCMSD plays significant roles in variations of aerosol optical properties and
388 estimations of DARF as well as the air heating rate caused by the existence of BC particles. It was
389 recommended that a real time measured BCMSD be used when estimating the aerosol DARF, instead
390 of a constant one. The BCMSD was as important as that of the BC mixing states.

391 5 Conclusions

392 Knowledge of the BC microphysical properties especially the size-dependent information can
393 help reduce the uncertainties when estimating the aerosol radiative effects. BCMSD is an important
394 quantity in its own right, being directly and indirectly applicable to determination the sources, aging
395 processes and mixing states of BC aerosols. In this study, the characteristics of BCMSD were studied
396 from the field measurement results by using our own developed measurement algorithm.

397 The BCMSD measurement system was developed and validated based on the works of Ning et al.
398 al. (2013) by using differential mobility analyzer (DMA) in tandem with Aethalometer (AE). When
399 deriving the BCMSD, a comprehensive multiple charging correction algorithm was proposed and
400 implied. This algorithm was validated by closure study between the measured total m_{BC} from AE33
401 and the m_{BC} integrated from the measured BCPMSD using the datasets from field measurements.
402 Results showed that the multiple charging corrections could significantly change the shapes and
403 magnitudes of the raw measured BCPMSD. The accurate BCPMSD characteristics could be obtained
404 by our proposed method in this paper.

405 The developed measurement system was employed in a field campaign in the North China Plain
406 from 21 March to 9 April in 2017. The BCMSD was found to have two quasi-lognormal modes with
407 peaks at around 150 nm and 500 nm, respectively. These two modes were consistent with the
408 previous measurement results by MOUDI (Wang et al., 2015; Hu et al., 2012). The amount of the BC
409 mass concentrations for the coarse mode peaks were about twice to that of the fine mode.



410 The characteristic of the BCMSD was studied by fitting the shape of BCMSD with a bi-normal
411 distribution. The relationships between the fitted D_m and GSD were statistically studied. During the
412 aging processing, the opposite trends for the D_m and GSD were found for coarser mode. This is the
413 first time that the coarser mode of the BCMSD were synthetically studied. The BCMSD of coarser
414 mode varied significantly under different pollution conditions with peak diameter changed between
415 430 and 580 nm. However, the relationship between the D_m and GSD for smaller mode BC aerosols
416 were more complex due to the complex sources.

417 When the BCMSD were changed with the polluted condition, the corresponding aerosol optical
418 properties changes significantly. Sensitivity studies found that the aerosol g varies from 0.617 to
419 0.649 due to the variations in BCMSD. Aerosol g was more sensitive to D_m when the geometric
420 mean diameter of the BCMSD is in the range of 300 nm and 370 nm. The SSA can changed from
421 0.86 to 0.93. The σ_{sca} experienced significant change with the variation of BCMSD from 264 Mm^{-1}
422 to 313 Mm^{-1} and the σ_{abs} changed in the range between 21.94 Mm^{-1} and 44.12 Mm^{-1} . The
423 corresponding BC MAC was calculated to be in the range between 4.75 and $9.56 \text{ m}^2/\text{g}$.

424 The variations in DARF were estimated due to the variations of the BCMSD by using the
425 SBDART model. Results showed that the DARF can varies by about 22.5% for different BCMSD
426 and the heating rate for different measured BCMSD conditions could change from 3.56 to 3.75,
427 corresponding to a variation of 5.23%. At the same time, the variations in DARF due to the
428 variations in the BC mixing state was estimated to be 21.5% and that of the heating rate is 6.05%.
429 Thus, the variations of the BCMSD may had significant influence on the aerosol radiative budget and
430 an accurate measurement of BCMSD was very necessary.

431

432 **Competing interests.** The authors declare that they have no conflict of interest.

433 **Data availability.** The data used in this study is available when requesting the authors.

434 **Author contributions.** GZ, CZ, JT and YK designed and conducted the experiments; CS, YY, CZ and GZ
435 discussed the results.

436 **Acknowledgments.** This work is supported by the National Key R&D Program of China (2016YFA0602001) and
437 the National Natural Science Foundation of China (41590872).

438

439 **References**



- 440 Babu, S. S., Sreekanth, V., Moorthy, K. K., Mohan, M., Kirankumar, N. V. P., Subrahmanyam, D. B.,
441 Gogoi, M. M., Kompalli, S. K., Beegum, N., Chaubey, J. P., Kumar, V. H. A., and Manchandab, R.
442 K.: Vertical profiles of aerosol black carbon in the atmospheric boundary layer over a tropical coastal
443 station: Perturbations during an annular solar eclipse, *Atmospheric Research*, 99, 471-478,
444 10.1016/j.atmosres.2010.11.019, 2011.
- 445 Bau, S., Bemer, D., Gripari, F., Appert-Collin, J.-C., and Thomas, D.: Determining the effective
446 density of airborne nanoparticles using multiple charging correction in a tandem DMA/ELPI setup,
447 *Journal of Nanoparticle Research*, 16, 10.1007/s11051-014-2629-2, 2014.
- 448 Bond, T. C., Doherty, S. J., Fahey, D. W., Forster, P. M., Berntsen, T., DeAngelo, B. J., Flanner, M.
449 G., Ghan, S., Karcher, B., Koch, D., Kinne, S., Kondo, Y., Quinn, P. K., Sarofim, M. C., Schultz, M.
450 G., Schulz, M., Venkataraman, C., Zhang, H., Zhang, S., Bellouin, N., Guttikunda, S. K., Hopke, P.
451 K., Jacobson, M. Z., Kaiser, J. W., Klimont, Z., Lohmann, U., Schwarz, J. P., Shindell, D., Storelvmo,
452 T., Warren, S. G., and Zender, C. S.: Bounding the role of black carbon in the climate system: A
453 scientific assessment, *J Geophys Res-Atmos*, 118, 5380-5552, 10.1002/jgrd.50171, 2013.
- 454 Cheng, Y. F., Su, H., Rose, D., Gunthe, S. S., Berghof, M., Wehner, B., Achtert, P., Nowak, A.,
455 Takegawa, N., Kondo, Y., Shiraiwa, M., Gong, Y. G., Shao, M., Hu, M., Zhu, T., Zhang, Y. H.,
456 Carmichael, G. R., Wiedensohler, A., Andreae, M. O., and Pöschl, U.: Size-resolved measurement of
457 the mixing state of soot in the megacity Beijing, China: diurnal cycle, aging and parameterization,
458 *Atmospheric Chemistry and Physics*, 12, 4477-4491, 10.5194/acp-12-4477-2012, 2012.
- 459 Cheng, Y. H., Liao, C. W., Liu, Z. S., Tsai, C. J., and Hsi, H. C.: A size-segregation method for
460 monitoring the diurnal characteristics of atmospheric black carbon size distribution at urban traffic
461 sites, *Atmospheric Environment*, 90, 78-86, 2014.
- 462 Cheng, Y. H., and Yang, L. S.: Characteristics of Ambient Black Carbon Mass and Size-Resolved
463 Particle Number Concentrations during Corn Straw Open-Field Burning Episode Observations at a
464 Rural Site in Southern Taiwan, *Int J Environ Res Public Health*, 13, 10.3390/ijerph13070688, 2016.
- 465 China, S., Mazzoleni, C., Gorkowski, K., Aiken, A. C., and Dubey, M. K.: Morphology and mixing
466 state of individual freshly emitted wildfire carbonaceous particles, *Nature communications*, 4, 2122,
467 2013.
- 468 Deng, Z. Z., Zhao, C. S., Ma, N., Liu, P. F., Ran, L., Xu, W. Y., Chen, J., Liang, Z., Liang, S., Huang,
469 M. Y., Ma, X. C., Zhang, Q., Quan, J. N., Yan, P., Henning, S., Mildenberger, K., Sommerhage, E.,



470 Schafer, M., Stratmann, F., and Wiedensohler, A.: Size-resolved and bulk activation properties of
471 aerosols in the North China Plain, *Atmospheric Chemistry and Physics*, 11, 3835-3846,
472 10.5194/acp-11-3835-2011, 2011.

473 Drinovec, L., Močnik, G., Zotter, P., Prévôt, A. S. H., Ruckstuhl, C., Coz, E., Rupakheti, M., Sciare,
474 J., Müller, T., Wiedensohler, A., and Hansen, A. D. A.: The "dual-spot" Aethalometer: an improved
475 measurement of aerosol black carbon with real-time loading compensation, *Atmospheric*
476 *Measurement Techniques*, 8, 1965-1979, 10.5194/amt-8-1965-2015, 2015.

477 Ferrero, L., Mocnik, G., Ferrini, B. S., Perrone, M. G., Sangiorgi, G., and Bolzacchini, E.: Vertical
478 profiles of aerosol absorption coefficient from micro-Aethalometer data and Mie calculation over
479 Milan, *Science of the Total Environment*, 409, 2824-2837, 10.1016/j.scitotenv.2011.04.022, 2011.

480 Gao, R. S., Schwarz, J. P., Kelly, K. K., Fahey, D. W., Watts, L. A., Thompson, T. L., Spackman, J. R.,
481 Slowik, J. G., Cross, E. S., Han, J. H., Davidovits, P., Onasch, T. B., and Worsnop, D. R.: A Novel
482 Method for Estimating Light-Scattering Properties of Soot Aerosols Using a Modified
483 Single-Particle Soot Photometer, *Aerosol Sci. Technol.*, 41, 125-135, 10.1080/02786820601118398,
484 2007.

485 Gong, X., Zhang, C., Chen, H., Nizkorodov, S. A., Chen, J., and Yang, X.: Size distribution and
486 mixing state of black carbon particles during a heavy air pollution episode in Shanghai, *Atmos.*
487 *Chem. Phys.*, 16, 5399-5411, 10.5194/acp-16-5399-2016, 2016.

488 Guo, Y.: Characteristics of size-segregated carbonaceous aerosols in the Beijing-Tianjin-Hebei
489 region, *Environ. Sci. Pollut. Res.*, 23, 13918-13930, 10.1007/s11356-016-6538-z, 2016.

490 Hagen, D. E., and Alofs, D. J.: Linear Inversion Method to Obtain Aerosol Size Distributions from
491 Measurements with a Differential Mobility Analyzer, *Aerosol Sci. Technol.*, 2, 465-475,
492 10.1080/02786828308958650, 2007.

493 Hansen, A. D. A., Rosen, H., and Novakov, T.: The aethalometer — An instrument for the real-time
494 measurement of optical absorption by aerosol particles, *Science of The Total Environment*, 36,
495 191-196, [http://dx.doi.org/10.1016/0048-9697\(84\)90265-1](http://dx.doi.org/10.1016/0048-9697(84)90265-1), 1984.

496 He, M., and Dhaniyala, S.: A multiple charging correction algorithm for scanning electrical mobility
497 spectrometer data, *Journal of Aerosol Science*, 61, 13-26, 10.1016/j.jaerosci.2013.03.007, 2013.

498 He, M., Dhaniyala, S., and Wagner, M.: Aerosol Filtration with Mobility-Classified Particles: Role of
499 Multiply Charged Particles in Skewing Penetration Measurements, *Aerosol Sci. Technol.*, 49,



- 500 704-715, 10.1080/02786826.2015.1062467, 2015.
- 501 Hu, M., Peng, J., Sun, K., Yue, D., Guo, S., Wiedensohler, A., and Wu, Z.: Estimation of
502 size-resolved ambient particle density based on the measurement of aerosol number, mass, and
503 chemical size distributions in the winter in Beijing, *Environ Sci Technol*, 46, 9941-9947,
504 10.1021/es204073t, 2012.
- 505 Huang, X.-F., Sun, T.-L., Zeng, L.-W., Yu, G.-H., and Luan, S.-J.: Black carbon aerosol
506 characterization in a coastal city in South China using a single particle soot photometer, *Atmospheric*
507 *Environment*, 51, 21-28, 10.1016/j.atmosenv.2012.01.056, 2012.
- 508 Huang, X. F., and Yu, J. Z.: Size distributions of elemental carbon in the atmosphere of a coastal
509 urban area in South China: characteristics, evolution processes, and implications for the mixing state,
510 *Atmospheric Chemistry and Physics*, 8, 5843-5853, 2008a.
- 511 Huang, X. F., and Yu, J. Z.: Size distributions of elemental carbon in a coastal urban atmosphere in
512 South China: characteristics, evolution processes, and implications for the mixing state, *Atmospheric*
513 *Chemistry & Physics*, 8, 5843-5853, 2008b.
- 514 Jacobson, M. Z.: Strong radiative heating due to the mixing state of black carbon in atmospheric
515 aerosols, *Nature*, 409, 695-697, 2001.
- 516 Janssen, N. A. H., Hoek, G., Simic-Lawson, M., Fischer, P., van Bree, L., ten Brink, H., Keuken, M.,
517 Atkinson, R. W., Anderson, H. R., Brunekreef, B., and Cassee, F. R.: Black Carbon as an Additional
518 Indicator of the Adverse Health Effects of Airborne Particles Compared with PM10 and PM2.5,
519 *Environ Health Persp*, 119, 1691-1699, 10.1289/ehp.1003369, 2011.
- 520 KlausWilleke, and Baron, P.: *Aerosol measurement : principles, techniques, and applications*, Van
521 Nostrand Reinhold, 807-808 pp., 1996.
- 522 Knutson, E. O., and Whitby, K. T.: Aerosol classification by electric mobility: apparatus, theory, and
523 applications, *Journal of Aerosol Science*, 6, 443-451, 1975.
- 524 Koch, D., Schulz, M., Kinne, S., and Mcnaughton, C.: Evaluation of black carbon estimations in
525 global aerosol models, *Atmospheric Chemistry & Physics*, 9, 9001-9026, 2009.
- 526 Koch, D., and Del Genio, A. D.: Black carbon semi-direct effects on cloud cover: review and
527 synthesis, *Atmos. Chem. Phys.*, 10, 7685-7696, 10.5194/acp-10-7685-2010, 2010.
- 528 Kuang, Y., Zhao, C. S., Tao, J. C., and Ma, N.: Diurnal variations of aerosol optical properties in the
529 North China Plain and their influences on the estimates of direct aerosol radiative effect, *Atmos.*



- 530 Chem. Phys., 15, 5761-5772, 10.5194/acp-15-5761-2015, 2015.
- 531 Kuang, Y., Zhao, C. S., Tao, J. C., Bian, Y. X., and Ma, N.: Impact of aerosol hygroscopic growth on
532 the direct aerosol radiative effect in summer on North China Plain, Atmospheric Environment, 147,
533 224-233, 2016.
- 534 Lippmann, M., and Albert, R. E.: The Effect of Particle Size on the Regional Deposition of Inhaled
535 Aerosols in the Human Respiratory Tract, American Industrial Hygiene Association Journal, 30,
536 257-275, 10.1080/00028896909343120, 1969.
- 537 Liu, D., Whitehead, J., Alfarra, M. R., Reyes-Villegas, E., Spracklen, Dominick V., Reddington,
538 Carly L., Kong, S., Williams, Paul I., Ting, Y.-C., Haslett, S., Taylor, Jonathan W., Flynn, Michael J.,
539 Morgan, William T., McFiggans, G., Coe, H., and Allan, James D.: Black-carbon absorption
540 enhancement in the atmosphere determined by particle mixing state, Nature Geoscience, 10, 184-188,
541 10.1038/ngeo2901, 2017.
- 542 Ma, N., Zhao, C. S., Müller, T., Cheng, Y. F., Liu, P. F., Deng, Z. Z., Xu, W. Y., Ran, L., Nekat, B.,
543 van Pinxteren, D., Gnauk, T., Müller, K., Herrmann, H., Yan, P., Zhou, X. J., and Wiedensohler, A.: A
544 new method to determine the mixing state of light absorbing carbonaceous using the measured
545 aerosol optical properties and number size distributions, Atmos. Chem. Phys., 12, 2381-2397,
546 10.5194/acp-12-2381-2012, 2012.
- 547 Matsui, H., Hamilton, D. S., and Mahowald, N. M.: Black carbon radiative effects highly sensitive to
548 emitted particle size when resolving mixing-state diversity, Nature communications, 9, 3446,
549 10.1038/s41467-018-05635-1, 2018.
- 550 Menon, S., Hansen, J., Nazarenko, L., and Luo, Y.: Climate effects of black carbon aerosols in China
551 and India, Science, 297, 2250-2253, 10.1126/science.1075159, 2002.
- 552 Moffet, R. C., amp, apos, Brien, R. E., Alpert, P. A., Kelly, S. T., Pham, D. Q., Gilles, M. K., Knopf,
553 D. A., and Laskin, A.: Morphology and mixing of black carbon particles collected in central
554 California during the CARES field study, Atmospheric Chemistry and Physics, 16, 14515-14525,
555 10.5194/acp-16-14515-2016, 2016.
- 556 Moteki, N., and Kondo, Y.: Dependence of Laser-Induced Incandescence on Physical Properties of
557 Black Carbon Aerosols: Measurements and Theoretical Interpretation, Aerosol Sci. Technol., 44,
558 663-675, Pii 924375405
559 10.1080/02786826.2010.484450, 2010.



- 560 Nichols, J. L., Owens, E. O., Dutton, S. J., and Luben, T. J.: Systematic review of the effects of black
561 carbon on cardiovascular disease among individuals with pre-existing disease, *International Journal*
562 *of Public Health*, 58, 707-724, 2013.
- 563 Ning, Z., Chan, K. L., Wong, K. C., Westerdahl, D., Močnik, G., Zhou, J. H., and Cheung, C. S.:
564 Black carbon mass size distributions of diesel exhaust and urban aerosols measured using differential
565 mobility analyzer in tandem with Aethalometer, *Atmospheric Environment*, 80, 31-40,
566 10.1016/j.atmosenv.2013.07.037, 2013.
- 567 Ohata, S., Moteki, N., and Kondo, Y.: Evaluation of a Method for Measurement of the Concentration
568 and Size Distribution of Black Carbon Particles Suspended in Rainwater, *Aerosol Sci. Technol.*, 45,
569 1326-1336, 2011.
- 570 Peng, J., Hu, M., Guo, S., Du, Z., Zheng, J., Shang, D., Levy Zamora, M., Zeng, L., Shao, M., Wu,
571 Y.-S., Zheng, J., Wang, Y., Glen, C. R., Collins, D. R., Molina, M. J., and Zhang, R.: Markedly
572 enhanced absorption and direct radiative forcing of black carbon under polluted urban environments,
573 *Proceedings of the National Academy of Sciences*, 201602310, 10.1073/pnas.1602310113, 2016.
- 574 Raatikainen, T., Brus, D., Hooda, R. K., Hyvärinen, A.-P., Asmi, E., Sharma, V. P., Arola, A., and
575 Lihavainen, H.: Size-selected black carbon mass distributions and mixing state in polluted and clean
576 environments of northern India, *Atmospheric Chemistry and Physics*, 17, 371-383,
577 10.5194/acp-17-371-2017, 2017.
- 578 Ramachandran, S., and Rajesh, T. A.: Black carbon aerosol mass concentrations over Ahmedabad, an
579 urban location in western India: Comparison with urban sites in Asia, Europe, Canada, and the
580 United States, *J Geophys Res-Atmos*, 112, Artn D06211
581 10.1029/2006jd007488, 2007.
- 582 Ramanathan, V., and Carmichael, G.: Global and regional climate changes due to black carbon,
583 *Nature Geoscience*, 1, 221-227, 10.1038/ngeo156, 2008.
- 584 Ran, L., Deng, Z., Xu, X., Yan, P., Lin, W., Wang, Y., Tian, P., Wang, P., Pan, W., and Lu, D.: Vertical
585 profiles of black carbon measured by a micro-aethalometer in summer in the North China Plain,
586 *Atmospheric Chemistry and Physics*, 16, 10441-10454, 10.5194/acp-16-10441-2016, 2016a.
- 587 Ran, L., Deng, Z. Z., Wang, P. C., and Xia, X. A.: Black carbon and wavelength-dependent aerosol
588 absorption in the North China Plain based on two-year aethalometer measurements, *Atmospheric*
589 *Environment*, 142, 132-144, 10.1016/j.atmosenv.2016.07.014, 2016b.



590 Reddington, C. L., McMeeking, G., Mann, G. W., Coe, H., Frontoso, M. G., Liu, D., Flynn, M.,
591 Spracklen, D. V., and Carslaw, K. S.: The mass and number size distributions of black carbon aerosol
592 over Europe, *Atmospheric Chemistry and Physics*, 13, 4917-4939, 10.5194/acp-13-4917-2013, 2013.
593 Ricchiazzi, P., Yang, S., Gautier, C., and Sowle, D.: SBDART: A Research and Teaching Software
594 Tool for Plane-Parallel Radiative Transfer in the Earth's Atmosphere, *Bulletin of the American
595 Meteorological Society*, 79, 2101-2114, 10.1175/1520-0477(1998)079<2101:sarats>2.0.co;2, 1998.
596 Roberts, G. C., Ramana, M. V., Corrigan, C., Kim, D., and Ramanathan, V.: Simultaneous
597 observations of aerosol-cloud-albedo interactions with three stacked unmanned aerial vehicles,
598 *Proceedings of the National Academy of Sciences of the United States of America*, 105, 7370-7375,
599 10.1073/pnas.0710308105, 2008.
600 Schwarz, J. P., Gao, R. S., Fahey, D. W., Thomson, D. S., Watts, L. A., Wilson, J. C., Reeves, J. M.,
601 Darbeheshti, M., Baumgardner, D. G., Kok, G. L., Chung, S. H., Schulz, M., Hendricks, J., Lauer, A.,
602 Kärcher, B., Slowik, J. G., Rosenlof, K. H., Thompson, T. L., Langford, A. O., Loewenstein, M., and
603 Aikin, K. C.: Single-particle measurements of midlatitude black carbon and light-scattering aerosols
604 from the boundary layer to the lower stratosphere, *Journal of Geophysical Research*, 111,
605 10.1029/2006jd007076, 2006.
606 Singh, S., Fiddler, M. N., and Bililign, S.: Measurement of size-dependent single scattering albedo of
607 fresh biomass
608 burning aerosols using the extinction-minus-scattering technique with a
609 combination of cavity ring-down spectroscopy and nephelometry, *Atmospheric Chemistry and
610 Physics*, 16, 13491-13507, 10.5194/acp-16-13491-2016, 2016.
611 Song, S., Wu, Y., Xu, J., Ohara, T., Hasegawa, S., Li, J., Yang, L., and Hao, J.: Black carbon at a
612 roadside site in Beijing: Temporal variations and relationships with carbon monoxide and particle
613 number size distribution, *Atmospheric Environment*, 77,
614 213-221, <https://doi.org/10.1016/j.atmosenv.2013.04.055>, 2013.
615 Stabile, L., Fuoco, F. C., and Buonanno, G.: Characteristics of particles and black carbon emitted by
616 combustion of incenses, candles and anti-mosquito products, *Building and Environment*, 56, 184-191,
617 10.1016/j.buildenv.2012.03.005, 2012.
618 Stevens, B., and Feingold, G.: Untangling aerosol effects on clouds and precipitation in a buffered
619 system, *Nature*, 461, 607-613, 10.1038/nature08281, 2009.



- 620 Tigges, L., Wiedensohler, A., Weinhold, K., Gandhi, J., and Schmid, H. J.: Bipolar charge
621 distribution of a soft X-ray diffusion charger, *Journal of Aerosol Science*, 90, 77-86,
622 10.1016/j.jaerosci.2015.07.002, 2015.
- 623 Turner, M. D., Henze, D. K., Hakami, A., Zhao, S. L., Resler, J., Carmichael, G. R., Stanier, C. O.,
624 Baek, J., Sandu, A., Russell, A. G., Nenes, A., Jeong, G. R., Capps, S. L., Percell, P. B., Pinder, R. W.,
625 Napelenok, S. L., Bash, J. O., and Chai, T. F.: Differences Between Magnitudes and Health Impacts
626 of BC Emissions Across the United States Using 12 km Scale Seasonal Source Apportionment,
627 *Environmental Science & Technology*, 49, 4362-4371, 10.1021/es505968b, 2015.
- 628 Venkataraman, C., and Friedlander, S. K.: Size distributions of polycyclic aromatic hydrocarbons and
629 elemental carbon. 2. Ambient measurements and effects of atmospheric processes, *Environmental
630 Science & Technology*, 28, 563, 1994.
- 631 Virkkula, A., Makela, T., Hillamo, R., Yli-Tuomi, T., Hirsikko, A., Hameri, K., and Koponen, I. K.: A
632 simple procedure for correcting loading effects of aethalometer data, *J Air Waste Manag Assoc*, 57,
633 1214-1222, 10.3155/1047-3289.57.10.1214, 2007.
- 634 Virkkula, A., Chi, X., Ding, A., Shen, Y., Nie, W., Qi, X., Zheng, L., Huang, X., Xie, Y., Wang, J.,
635 Petaja, T., and Kulmala, M.: On the interpretation of the loading correction of the aethalometer,
636 *Atmospheric Measurement Techniques*, 8, 4415-4427, 10.5194/amt-8-4415-2015, 2015.
- 637 Wang, Q. Y., Huang, R. J., Cao, J. J., Tie, X. X., Ni, H. Y., Zhou, Y. Q., Han, Y. M., Hu, T. F., Zhu, C.
638 S., Feng, T., Li, N., and Li, J. D.: Black carbon aerosol in winter northeastern Qinghai-Tibetan
639 Plateau, China: the source, mixing state and optical property, *Atmospheric Chemistry and Physics*,
640 15, 13059-13069, 10.5194/acp-15-13059-2015, 2015.
- 641 Wex, H., Neusüß, C., Wendisch, M., Stratmann, F., Koziar, C., Keil, A., Wiedensohler, A., and Ebert,
642 M.: Particle scattering, backscattering, and absorption coefficients: An in situ closure and sensitivity
643 study, *Journal of Geophysical Research: Atmospheres*, 107, LAC 4-1-LAC 4-18,
644 10.1029/2000jd000234, 2002.
- 645 Wiedensohler, A.: An approximation of the bipolar charge distribution for particles in the submicron
646 size range, *Journal of Aerosol Science*, 19, 387-389, 1988.
- 647 Wiedensohler, A., and Fissan, H. J.: Aerosol charging in high purity gases, *Journal of Aerosol
648 Science*, 19, 867-870, 1988.
- 649 Wilcox, E. M., Thomas, R. M., Praveen, P. S., Pistone, K., Bender, F. A. M., and Ramanathan, V.:



650 Black carbon solar absorption suppresses turbulence in the atmospheric boundary layer, Proceedings
651 of the National Academy of Sciences, 113, 11794-11799, 10.1073/pnas.1525746113, 2016.

652 Wu, Y., Cheng, T., Zheng, L., and Chen, H.: Effect of morphology on the optical properties of soot
653 aggregated with spheroidal monomers, *Journal of Quantitative Spectroscopy & Radiative Transfer*,
654 168, 158-169, 2016a.

655 Wu, Y., Wang, X., Tao, J., Huang, R., Tian, P., Cao, J., Zhang, L., Ho, K.-F., and Zhang, R.: Size
656 distribution and source of black carbon aerosol in
657 urban Beijing during winter haze episodes, *Atmospheric Chemistry and Physics Discussions*, 1-25,
658 10.5194/acp-2016-1096, 2016b.

659 Wu, Y., Cheng, T., Liu, D., Allan, J. D., Zheng, L., and Chen, H.: Light Absorption Enhancement of
660 Black Carbon Aerosol Constrained by Particle Morphology, *Environ Sci Technol*, 52, 6912-6919,
661 10.1021/acs.est.8b00636, 2018.

662 Xiaofeng Huang, Zhen Yu, † Jian, Lingyan He, A., and Min, H.: Size Distribution Characteristics of
663 Elemental Carbon Emitted from Chinese Vehicles: Results of a Tunnel Study and Atmospheric
664 Implications, *Environmental Science & Technology*, 40, 5355-5360, 2006.

665 Yu, H., and Yu, J. Z.: Modal Characteristics of Elemental and Organic Carbon in an Urban Location
666 in Guangzhou, China, *Aerosol Sci. Technol.*, 43, 1108-1118, 2009.

667 Yu, H., Wu, C., Wu, D., and Yu, J. Z.: Size distributions of elemental carbon and its contribution to
668 light extinction in urban and rural locations in the pearl river delta region, China, *Atmos. Chem.*
669 *Phys.*, 10, 5107-5119, 10.5194/acp-10-5107-2010, 2010.

670 Zhang, R., Khalizov, A. F., Pagels, J., Zhang, D., Xue, H., and McMurry, P. H.: Variability in
671 morphology, hygroscopicity, and optical properties of soot aerosols during atmospheric processing,
672 *Proceedings of the National Academy of Sciences of the United States of America*, 105,
673 10291-10296, 10.1073/pnas.0804860105, 2008.

674 Zhang, Y., Zhang, Q., Cheng, Y., Su, H., Kecorius, S., Wang, Z., Wu, Z., Hu, M., Zhu, T.,
675 Wiedensohler, A., and He, K.: Measuring the morphology and density of internally mixed black
676 carbon with SP2 and VTDMA: new insight into the absorption enhancement of black carbon in the
677 atmosphere, *Atmospheric Measurement Techniques*, 9, 1833-1843, 10.5194/amt-9-1833-2016, 2016.

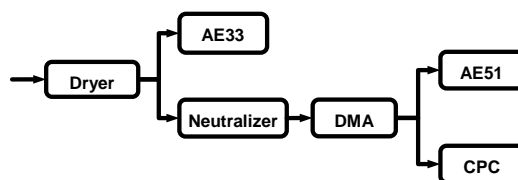
678 Zhao, G., Zhao, C., Kuang, Y., Bian, Y., Tao, J., Shen, C., and Yu, Y.: Calculating the aerosol
679 asymmetry factor based on measurements from the humidified nephelometer system, *Atmospheric*



680 Chemistry and Physics, 18, 9049-9060, 10.5194/acp-18-9049-2018, 2018.

681

682

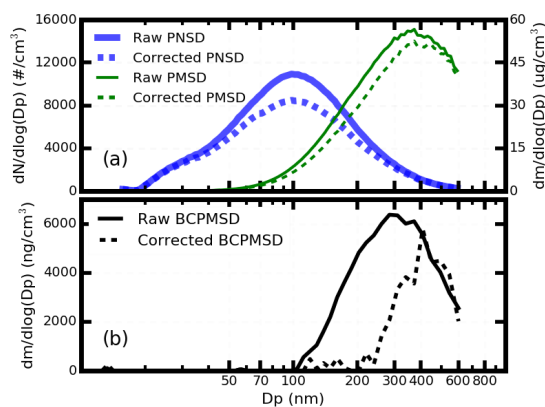


683

684

685

Figure 1. The schematic diagram of the instrument setup.

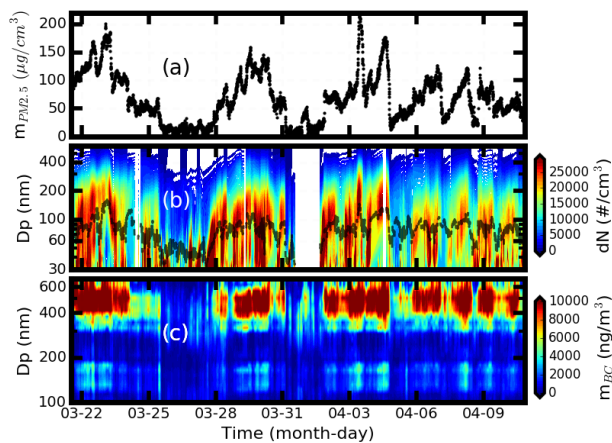


686

687 **Figure 2.** Case of multiple charging correction processing. (a) the multiple charging correction of the
688 aerosol PNSD and aerosol PMSD, (b) the multiple charging correction of the BCPMSD. The solid
689 line is the measured results without multiple charging corrections and the dotted line is the multiple
690 charging corrections results.

691

692

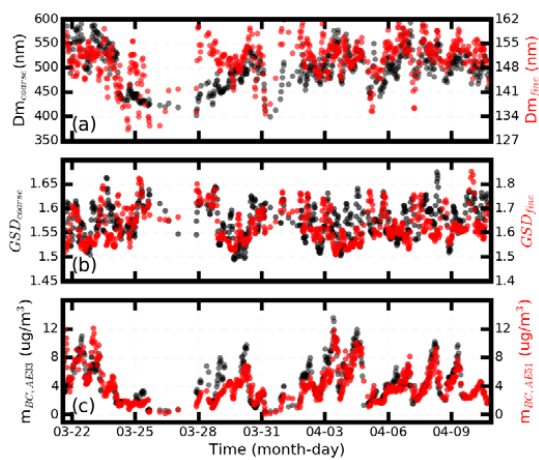


693

694 **Figure 3.** The measured time series of mass concentrations for (a) the PM2.5; (b) the aerosol
695 PNSD in filled color, the geometric median diameter in dotted line; and (c) the BCMSD.

696

697



698

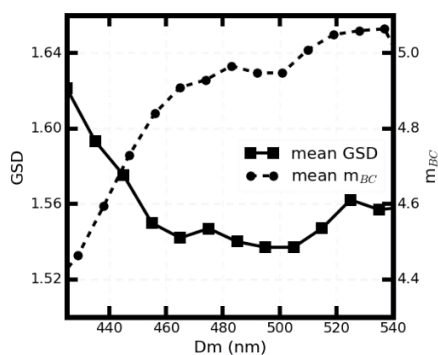
699 **Figure 4.** The (a) D_m and (b) GSD of the BCMSD at coarse mode (black) and fine mode (red); (c)
700 measured m_{BC} by AE33 (black) and measured m_{BC} from integrated m_{BC} of the BCMSD from AE51.

701

702



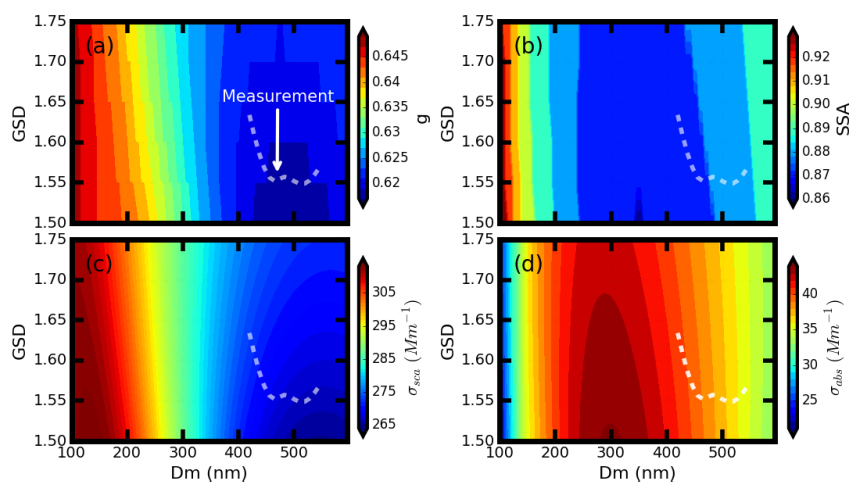
703



704

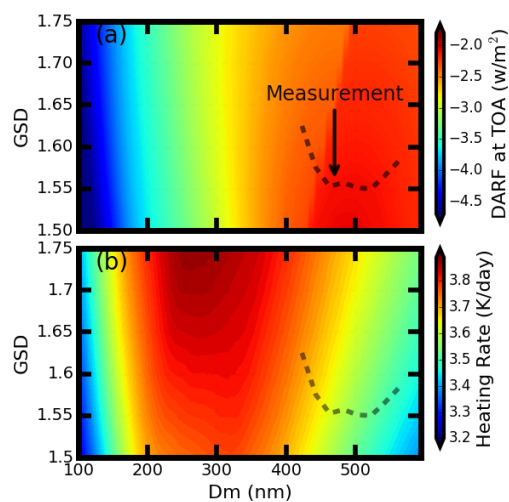
705 **Figure 5.** The relationship between the D_m and the GSD. The black dots show the real measured D_m
706 and GSD. The black line shows the mean results of the GSD for different D_m . The black line marked
707 with square shows the variation of mean m_{BC} with the D_m .

708



709 **Figure 6.** Variations of aerosol optics properties under different BCMSD conditions, which are
710 represented by different Dm and GSD values: (a) aerosol asymmetry factor, (b) single scatter albedo,
711 (c) scattering coefficient and (d) extinction coefficient . The grey dotted line in the figure shows the
712 evolution path of the BCMSD according to results of field measurements.

713



714

715 **Figure 7.** Variations of (a) DARF and (b) heating rate under different BCMSD conditions, which are
716 represented by different Dm and GSD values. The black dotted line in the figure shows the evolution
717 path of the BCMSD according to results of field measurements.

718



719 **Table 1.** Comparison of the DARF and heating rate values under different BC mixing states and
720 different BCMSD conditions.

		Mixing State			BCMSD	
		Internal	External	Core-Shell	Minimum	Maximum
DARF	Value(w/m^2)	-2.31	-2.57	-2.81	-2.50	-2.04
	Variation	21.5%			22.5%	
Heat Rate	Value(K/day)	3.67	3.47	3.68	3.56	3.75
	Variation	6.05%			5.23%	

721